This version of the article has been accepted for publication, after peer review (when applicable) and is subject to Springer Nature's AM terms of use, but is not the Version of Record and does not reflect post-acceptance improvements, or any corrections. The Version of Record is available online at:
https://doi.org/10.1557/s43580-022-00453-6

Parasitic Side Channel Formation Due to Ion Implantation Isolation of GaN HEMT

Hao Yu[1,*], Uthayasankaran Peralagu[1], Alireza Alian[1], Ming Zhao[1], Bertrand Parvais[1,2], and Nadine Collaert[1]

[1]*imec, Kapeldreef 75, Heverlee, Belgium*

[2]*Vrije Universiteit Brussels, Dept. ETRO, Belgium*

[*]hao.yu@imec.be

Abstract: Low-dose high-energy ion implantation is effective for isolating GaN high-electron-mobility transistors (HEMTs). However, lateral penetration of implanted ions induces damages at sides of AlGaN/AlN/GaN HEMTs and cause parasitic channel formation. By comparing ion implantation isolated HEMTs with varied widths, the parasitic channel behaviour is characterized: the parasitic channel shows low on-state conductance, reduced gate current, and more positive threshold voltage compared to the active HEMT channel. The high N ion implantation energy for HEMT isolation was up to 375 keV, and the effective widths of HEMTs are narrowed by ~0.5 μm. The electrical characteristics of the parasitic channel are theoretically understood by considering ionization of point defect generated in the AlGaN/AlN/GaN heterostructures.

1. Introduction

Ion implantation has been a widely applied isolation technique for wide bandgap semiconductors [1], [2]. Comprehensive knowledge of the mechanism of ion implantation isolation for GaN HEMTs makes room for refinement. Good knowledge of ion implantation induced defect formation helps understand those isolation regions induced reliability weaknesses in GaN transistors [3]. In a recent study [4], we report that the sheet resistance R_{sh} of the isolation region—a key indicator of isolation quality—is determined by an interplay between net polarization charges in GaN heterostructures and the point defects generated by ion implantation. This explains why the R_{sh} of isolated GaN heterostructures depend only weakly on ion species but strongly on post-isolation thermal budget [4]–[9] (Fig. 1a). The ion implantation isolation has commonly been applied with a low-ion-dose (<10^{14} cm^{-2}) high-ion-energy (of tens to hundreds of eV) condition. Under such conditions, the isolated GaN is abundant with point defects but free with significant extended defects or amorphization [2]. The point defects effectively remove free carriers in the GaN but are prone to recombination at high temperatures. Therefore, a low

post-ion implantation thermal budget is necessary to guarantee high isolation quality between the active GaN HEMTs (Fig. 1a).

The isolation and leakage mechanisms of ion implantation isolated GaN heterostructures [1] can be understood by introducing native point defect (Al, Ga, N vacancies and interstitials) with specific energy levels [10] into the energy band diagram (Fig. 1b). The constructed energy band diagrams provide a good explanation of the dependence of R_{sh} in the isolation regions on barrier thicknesses of the heterostructures [4].

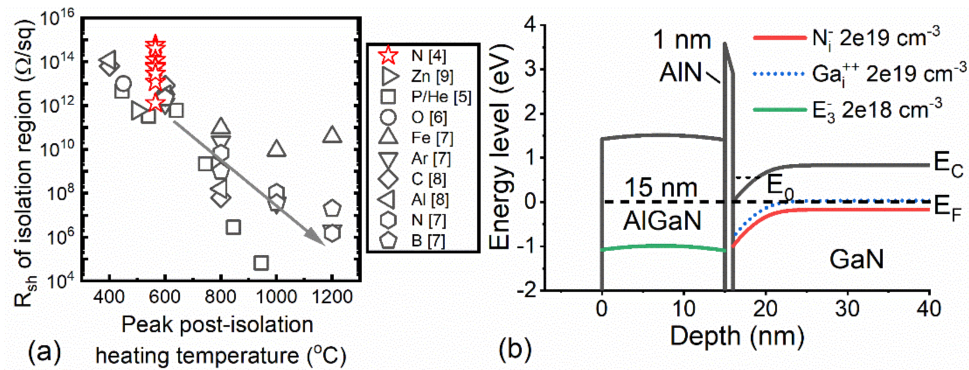

Fig. 1 (a) Benchmarks of R_{sh} of AlGaN/(AlN/)GaN heterostructures as a function of post-isolation processing temperature. (b) Simulated energy band diagram of ion implantation isolated AlGaN/AlN/GaN heterostructure [4].

Note that the ion implantation isolation region does not form sharp interfaces with active regions of GaN HEMTs. Inevitable lateral ion penetration generates defects and causes parasitic channel formation at the sides of GaN HEMTs. In this work, we analyse the characteristics of the parasitic GaN channel at the sides of AlGaN/AlN/GaN HEMTs. With the knowledge gained about isolated AlGaN/AlN/GaN heterostructures in our previous work [4], the characteristics of the parasitic side channels are theoretically explained by the point defect behaviour. This study complements literature knowledge of ion implantation impacts on HEMT behaviour [11]–[13].

2. Experimental

AlGaN/AlN/GaN structures were grown by MOCVD on high-resistivity 200 mm Si (111). The epitaxial buffer consists of AlN nucleation layer, AlGaN and AlGaN/AlN superlattice layers, and a 1 um thick C-doped GaN layer [14]. A 300 nm unintentionally doped GaN channel layer (i-GaN) is grown on top of the buffer layers. Then a 1 nm AlN interlayer and a 15 nm AlGaN top barrier are grown on top of the i-GaN. The AlGaN surfaces of all samples were in-situ passivated with 5 nm SiN and ex-situ capped with extra 150 nm thick dielectrics. The SiN/AlGaN interface state density is ~3×10^{12} eV^{-1}cm^{-2}[15]. Next, the active regions of all samples were covered

with photoresist, while the isolation regions received three steps of N ion implantation with ion energies and doses of 75 keV 8×10^{12} cm^{-2}, 150 keV 2×10^{13} cm^{-2}, and 375 keV 3×10^{13} cm^{-2}, respectively. After the N ion implantation isolation, 0.8~10 μm wide HEMTs with the same 0.13 μm gate length were fabricated. The gate-to-source and gate-to-drain distances were 1.5 μm and 1.75 μm, respectively. There was no intentional annealing after the N ion implantation. The highest thermal budget that the isolation region received was 565°C 90s annealing in N_2 for HEMT ohmic contact formation. The rest of the post-isolation processing of our devices, including back-end-of-line (BEOL) steps, features low temperature below 500°C [16]. Current-voltage measurements of HEMTs were performed with a Keysight B1500A semiconductor device parameter analyzer. The profile of the N ion and the associated interstitial/vacancy were calculated with the Transport of Ions in Matter (TRIM) Monte Carlo simulator [17] (Fig. 2a).

3. Results and discussions

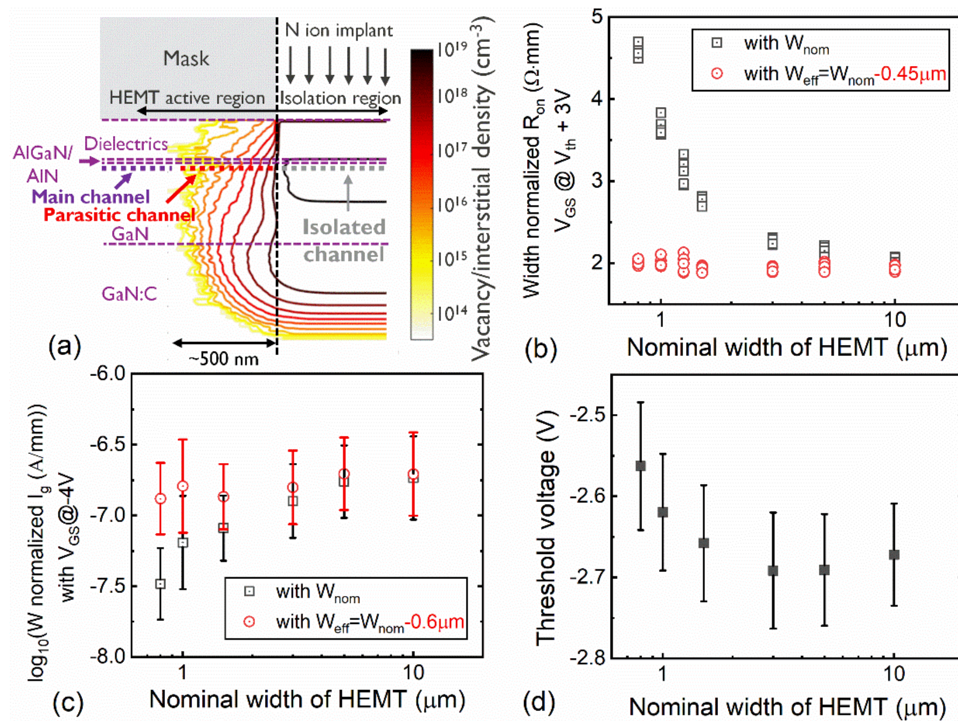

Fig. 2 (a) Ion implantation induced point defect generation at a HEMT side. Distribution and density of point defects are simulated by TRIM. Magnitude of point defect density is calibrated according to experimental values from isolation region [4]. (b) R_{on}, (c) I_g, (d) V_{th} as a function of the W_{nom} of HEMTs. The (b) R_{on}, (c) I_g are normalized by W_{nom} or W_{eff}.

The TRIM simulation provides three-dimensional Monte-Carlo simulation of ion collision events, which further contributes to a two-dimensional point defect distribution in Fig. 2a. Since annihilation of point defects by dynamic annealing and thermal annealing are not simulated by the TRIM [17], the direct outcome point defect

densities from TRIM are much overestimated and thus only provide theoretical guidance. As an attempt for correction, we calibrate the point defect density in Fig. 2a according to our experimentally extracted value from the isolation region [18]: 100 times lower point defect density is plotted in Fig. 2a based on original TRIM results. Observed from the point defect distribution, clearly, the implanted N ions laterally penetrate the GaN HEMT active region and generate point defects at the sides of HEMTs with a tailing profile: defective side parasitic channels form as a result. In Fig. 2b and Fig. 2c, by comparing HEMT on-stage resistances (R_{on}) and gate leakage (I_g) with varied widths, we observe that the parasitic side channels have reduced on-state conductance and reverse bias gate leakage compared to the unimplanted channel region. These effects can be described as narrowing of effective widths (W_{eff}) of HEMTs compared to their nominal widths (W_{nom}). Furthermore, for very narrow HEMTs ($W_{nom} \leq 1\mu m$) whose parasitic channels dominate the HEMT behaviour, we observe an increase of the HEMT threshold voltage V_{th} in Fig. 2d. Interpretation of these characteristics of parasitic side channels induced by lateral ion penetration requires knowledge of the ion implantation induced defect behaviour in the AlGaN/GaN heterostructure.

In our previous work [4], we manage to estimate a point defect density of $>1\times10^{19}$ cm^{-3} in the GaN and $>1\times10^{18}$ cm^{-3} in the AlGaN in the N ion implantation isolation region. Simple assumptions are made in [4] to describe the electrical behaviour of the HEMT isolation region: Fermi-level pinning in the isolated GaN is governed by the N_i^- interstitial acceptors and the Ga_i^{++} interstitial double donors [1], [10], whose energy levels locate at 1.0 eV and 0.8 eV respectively below the GaN conduction band minimum E_C; an imaginary acceptor E_3^- at 2.5 eV below the E_C of the AlGaN is introduced to describe the net negative charges observed from the implanted AlGaN. The energy band diagram simulated in the Fig. 1b has helped well describe the leakage behaviour in the HEMT isolation [4]. Knowledge of the HEMT isolation region sheds light upon the characteristics of the HEMT parasitic side channels. The point defect density in the parasitic side channel would gradually ramp down from 1×10^{19} cm^{-3} with an increased distance from the nominal active/isolation region boundary. We carry out theoretical calculations in Fig. 3 and construct energy band diagrams in Fig. 4 to help interpret how a moderate amount of the N_i^- acceptor, $the\ Ga_i^{++}$ donor, and the E_3^- acceptor determine the parasitic channel characteristics.

The on-state conductance degradation of the parasitic channel is caused by both two dimensional electron gas (2DEG) density N_{sh} and mobility μ degradation. In Fig. 3a, the impact of defect density on N_{sh} is calculated by heterostructure energy band diagram construction [4], [15]. In Fig. 4a and Fig. 4b, we compare the energy band diagrams of a defect-free heterostructure to one containing a moderate amount of point defects. The acceptors N_i^-

in the GaN and E_3^- in the AlGaN cause the reduced 2DEG N_{sh}. In Fig. 3b, the defect density increased Coulomb scattering and μ degradation are calculated with a method in [19].

The reduced reverse-bias leakage current I_g of the parasitic channel is explained by a reduced electric field E_b in the AlGaN barrier. The reverse-bias I_g of AlGaN/GaN HEMT is commonly governed either by Poole-Frenkel (PF) emission or Fowler-Nordheim (FN) tunneling [20]. The I_g increases with E_b under both PF emission and FN tunnelling regimes. In Fig. 4c and Fig. 4d, we simulate the off-state energy band diagrams of a defect-free and a defective heterostructure at the same reverse gate bias voltage. A reduced E_b near the AlGaN barrier surface is observed in the defective heterostructure because the ionized acceptors lift the potential energy near the 2DEG channel. In Fig. 3c, by constructing energy band diagrams under the same V_g = -2.5 V condition, we calculate the decreased E_b at the gate AlGaN barrier surface with an increased point defect density.

The positive V_{th} shift of the parasitic channel is also caused by the ionized defect charges near the 2DEG channel. At the V_{th} condition, the Fermi level is above the defect charge neutrality level in the GaN. This corresponds to a net negative charge density near the GaN surface and a positive V_{th} shift. In Fig. 3d, we calculate the increased V_{th} with the point defect density in the heterostructure.

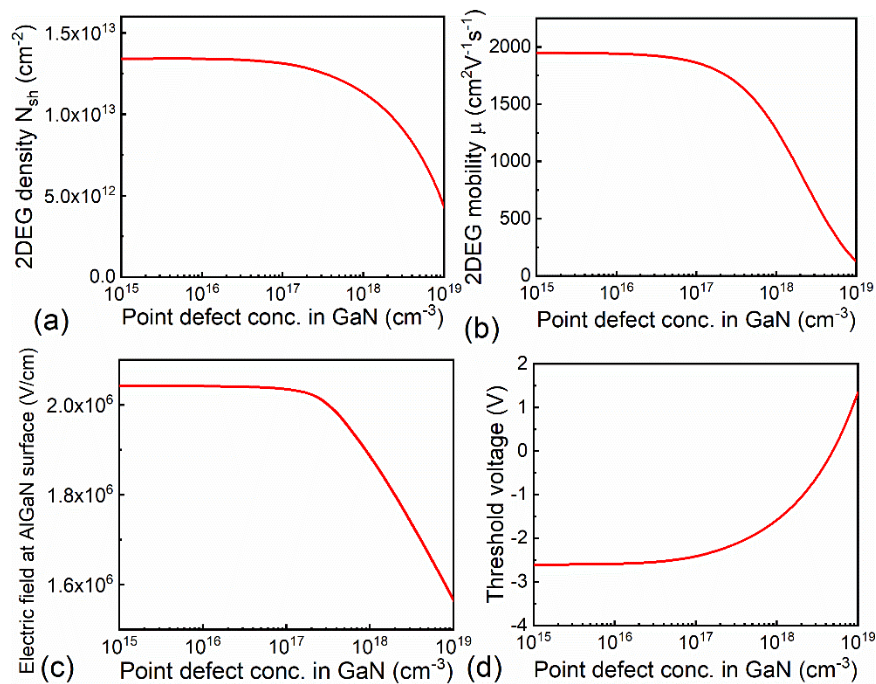

Fig. 3 Calculated (a) 2DEG N_{sh}, (b) 2DEG μ, (c) AlGaN surface E_b at the gate region with -2.5V gate bias, and (d) threshold voltage of a defective HEMT as a function of point defect density in GaN. The total point defect density in GaN includes that of both N_i^-, and Ga_i^{++}. N_i^-, Ga_i^{++}, and E_3^- are simulated with a constant density ratio of 1:1:10.

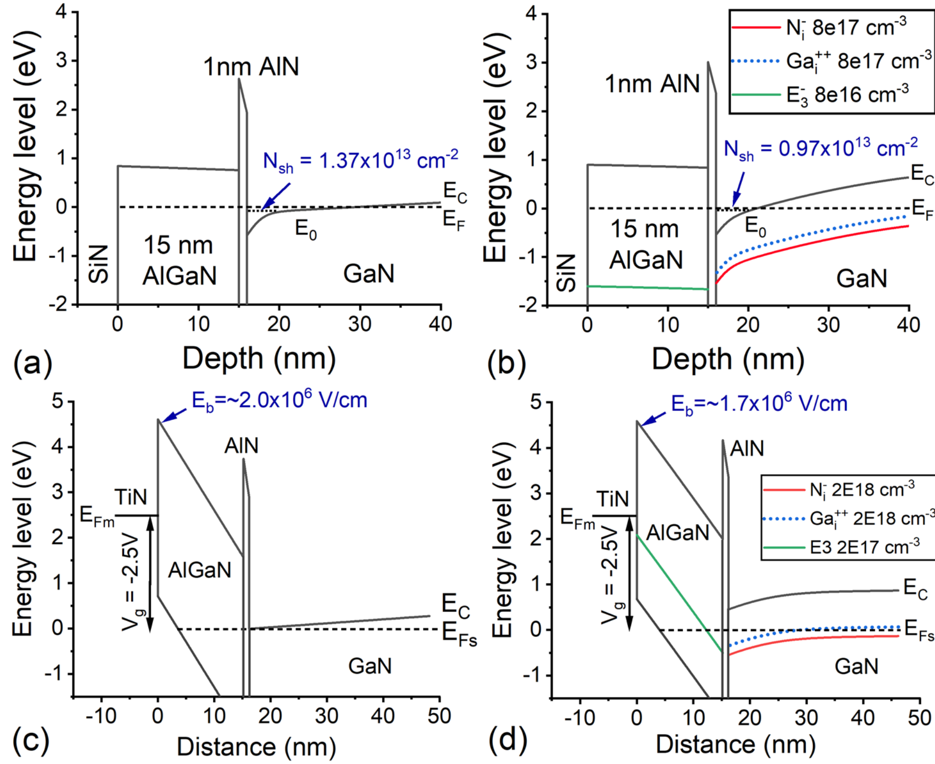

Fig. 4 Energy band diagrams of (a)(c) defect-free and (b)(d) a heterostructure containing moderate amount of point defects. (a)(b) are simulated for heterostructures in HEMT access regions at equilibrium; (c)(d) are simulated for heterostructures in HEMT gate region with -2.5V gate bias voltage.

Characteristics of the parasitic side channel are qualitatively explained by theoretical calculations and energy band diagram construction. According to theoretical calculation, we expect significant impacts of point defects on parasitic channel performance when the point defect density is above 10^{17} cm^{-3}; it corresponds to a 200~300 nm width near the boundary of isolated/active regions in Fig. 2a. This nicely explains a 0.45~0.6 μm W_{eff} narrowing of HEMT electrical performance in Fig. 2. Since an individual GaN HEMT width in a multi-finger RF device is usually 10~100 μm, the side isolation induced active HEMT width narrowing corresponds to 0.5~5 % performance reduction and is thus insignificant for this perspective. But the present work brings awareness of side point defect-rich regions to ion implantation isolated HEMTs; those defective parasitic side channels may lead into reliability concerns under high voltage stress. The reliability concern of the defective parasitic side channel deserves future investigations, since GaN HEMTs are frequently applied in high power conditions.

4. Conclusions

High-energy ion implantation isolation for GaN HEMTs causes parasitic defective channel formation at sides of HEMTs. We extract the parasitic channel characteristics from width dependence of HEMT. Assuming consistent point defect behaviour between the isolation region and the parasitic channel, we simulate the energy

band diagram of an ion damaged AlGaN/AlN/GaN heterostructure by considering two point defect levels in the GaN channel and one in the AlGaN barrier. We successfully interpret the parasitic channel characteristics by theoretical calculation and by constructed energy band diagrams of heterostructures.

Conflict of Interest Statement: No funds, grants, or other support was received

Data Availability Statement: The datasets generated during and/or analyzed during the current study are available from the corresponding author on reasonable request.

References

[1] S. J. Pearton, C. B. Vartuli, J. C. Zolper, C. Yuan, and R. A. Stall, "Ion implantation doping and isolation of GaN," *Appl Phys Lett*, vol. 67, no. March 1995, p. 1435, 1995, doi: 10.1063/1.114518.

[2] S. O. Kucheyev, J. S. Williams, J. Zou, C. Jagadish, and G. Li, "Ion implantation into GaN," *Materials Science and Engineering R*, vol. 33, pp. 51–107, 2001, doi: 10.1016/S0168-583X(00)00672-8.

[3] A. N. Tallarico *et al.*, "Gate Reliability of p-GaN HEMT with Gate Metal Retraction," *IEEE Trans Electron Devices*, vol. 66, no. 11, pp. 4829–4835, Nov. 2019, doi: 10.1109/TED.2019.2938598.

[4] H. Yu *et al.*, "Leakage mechanism in ion implantation isolated AlGaN/GaN heterostructures," *J Appl Phys*, vol. 131, no. 3, Jan. 2022, doi: 10.1063/5.0076243.

[5] G. Hanington *et al.*, "P/He ion implant isolation technology for AlGaN/GaN HFETs," *Electron Lett*, vol. 34, no. 2, pp. 193–195, 1998, doi: 10.1049/el:19980091.

[6] T. Oishi *et al.*, "Highly resistive GaN layers formed by ion implantation of Zn along the c axis," *J Appl Phys*, vol. 94, no. 3, pp. 1662–1666, 2003, doi: 10.1063/1.1590412.

[7] J. Y. Shiu *et al.*, "Oxygen ion implantation isolation planar process for AlGaN/GaN HEMTs," *IEEE Electron Device Letters*, vol. 28, no. 6, pp. 476–478, 2007, doi: 10.1109/LED.2007.896904.

[8] H. Umeda, T. Takizawa, Y. Anda, T. Ueda, and T. Tanaka, “High-voltage isolation technique using fe ion implantation for monolithic integration of AlGaN/GaN transistors,” *IEEE Trans Electron Devices*, vol. 60, no. 2, pp. 771–775, 2013, doi: 10.1109/TED.2012.2230264.

[9] A. Taube *et al.*, “Ion implantation for isolation of AlGaN/GaN HEMTs using C or Al,” *Physica Status Solidi (A) Applications and Materials Science*, vol. 212, no. 5, pp. 1162–1169, 2015, doi: 10.1002/pssa.201431724.

[10] A. Y. Polyakov, S. J. Pearton, P. Frenzer, F. Ren, L. Liu, and J. Kim, “Radiation effects in GaN materials and devices,” *J Mater Chem C Mater*, vol. 1, no. 5, pp. 877–887, 2013, doi: 10.1039/c2tc00039c.

[11] S. R. Challa *et al.*, “Understanding High-Energy 75-MeV Sulfur-Ion Irradiation-Induced Degradation in GaN-Based Heterostructures: The Role of the GaN Channel Layer,” *IEEE Trans Electron Devices*, vol. 68, no. 1, pp. 24–28, 2021, doi: 10.1109/TED.2020.3037259.

[12] N. A. Vega *et al.*, “Outstanding Reliability of Heavy-Ion-Irradiated AlInN/GaN on Silicon HFETs,” *IEEE Trans Nucl Sci*, vol. 66, no. 12, pp. 2417–2421, 2019, doi: 10.1109/TNS.2019.2954216.

[13] G. Sonia *et al.*, “Proton and heavy ion irradiation effects on AlGaN/GaN HFET devices,” *IEEE Trans Nucl Sci*, vol. 53, no. 6, pp. 3661–3666, 2006, doi: 10.1109/TNS.2006.885006.

[14] U. Peralagu *et al.*, “CMOS-compatible GaN-based devices on 200mm-Si for RF applications: integration and performance,” in *International Electron Devices Meeting, IEDM*, 2019, pp. 398–401. doi: 10.1109/IEDM19573.2019.8993582.

[15] H. Yu *et al.*, “Surface State Spectrum of AlGaN/AlN/GaN Extracted from Static Equilibrium Electrostatics,” *IEEE Trans Electron Devices*, vol. 68, no. 11, pp. 5559–5564, Nov. 2021, doi: 10.1109/TED.2021.3115086.

[16] B. Parvais *et al.*, “Advanced Transistors for High Frequency Applications,” *ECS Trans*, vol. 97, no. 5, pp. 27–38, Apr. 2020, doi: 10.1149/09705.0027ecst.

[17] J. F. Ziegler, M. D. Ziegler, and J. P. Biersack, “SRIM - The stopping and range of ions in matter (2010),” *Nucl Instrum Methods Phys Res B*, vol. 268, no. 11–12, pp. 1818–1823, 2010, doi: 10.1016/j.nimb.2010.02.091.

[18] H. Yu *et al.*, “Thermal budget increased alloy disorder scattering of 2DEG in III-N heterostructures,” *Appl Phys Lett*, vol. 120, no. 21, May 2022, doi: 10.1063/5.0093839.

[19] K. Lee, M. S. Shur, T. J. Drummond, and H. Morkoç, “Low field mobility of 2-d electron gas in modulation doped Al xGa1-xAs/GaAs layers,” *J Appl Phys*, vol. 54, no. 11, pp. 6432–6438, 1983, doi: 10.1063/1.331922.

[20] S. Turuvekere, D. S. Rawal, A. Dasgupta, and N. Dasgupta, “Evidence of Fowler-Nordheim tunneling in gate leakage current of AlGaN/GaN HEMTs at room temperature,” *IEEE Trans Electron Devices*, vol. 61, no. 12, pp. 4291–4294, Dec. 2014, doi: 10.1109/TED.2014.2361436.